Dear Author:

Your proofs are presented in a new design for all AGU journal articles.

The previous layout was designed more than a decade ago to support a print workflow and reading papers in hard copy. The design included text in two columns, and the PDF lacked any links. Starting in 2014, AGU will no longer provide individual print subscriptions to its journals. While some reading is done using a hard copy of the PDF, increasingly papers are read online on a variety of devices.

Because of these recent changes in reading habits and new technologies, AGU is implementing a new PDF design that aims to support both online and hard-copy reading and browsing. The main text is one column, to simplify scrolling online and viewing on devices with small screens. The column is not the full width of the page; this simplifies reading when the paper is printed, and allows notes to be added in the margins. Elements within the PDF link back to the full online version, the journal, and the AGU website, and the journal graphics are consistent across the PDF and website. In addition, links are provided to email the corresponding author and to access any supporting information. Links are also provided to references when DOIs are available. If a paper is part of a special section, a link is also provided to the main index page. Figures and tables can be sized as full-width when needed. Finally, the PDF contains metadata that can be exported.

To support the new PDF model, AGU has moved to a new excess page length calculation, described here:

http://publications.agu.org/author-resource-center/author-guide/publication-fees/

This will be implemented such that you will not incur additional excess length charges based on this new design.

This design will take effect across all AGU titles starting in 2014. Your feedback is welcome.

Thank you for publishing with AGU.

Sincerely,

Brooks Hanson
Director, Publications AGU
bhanson@agu.org

2000 Florida Avenue, NW, Washington, DC 20009-1277
Tel: 202.462.6900
Fax: +1 202.328.0566
www.agu.org

SPi	Journal Code:				Article ID					Dispatch: 18.01.14	CE: LGG
	J	G	R	A	5	0	7	9	1	No. of Pages: 20	ME:

AGU PUBLICATIONS

JGR

Journal of Geophysical Research: Space Physics

RESEARCH ARTICLE

10.1002/2013JA019354

Key Points:
- Entropy conservation in PIC simulation supports substorm onset concept
- Energy transfer dominated by conversion of Poynting flux to enthalpy flux
- Pre-reconnection thin current sheets may be the driver of onset arcs

Correspondence to:
J. Birn,
jbirn@lanl.gov

Citation:
Birn, J., and M. Hesse (2014), Forced reconnection in the near magnetotail: Onset and energy conversion in PIC and MHD simulations, *J. Geophys. Res. Space Physics*, *119*, doi:10.1002/2013JA019354.

Received 20 AUG 2013
Accepted 2 JAN 2014
Accepted article online 6 JAN 2014

Forced reconnection in the near magnetotail: Onset and energy conversion in PIC and MHD simulations

J. Birn[1,2] and M. Hesse[3]

[1]Space Science Institute, Boulder, Colorado, USA, [2]Los Alamos National Laboratory, Los Alamos, New Mexico, USA, [3]NASA/Goddard Space Flight Center, Greenbelt, Maryland, USA

Abstract Using two-dimensional particle-in-cell (PIC) together with magnetohydrodynamic (MHD) simulations of magnetotail dynamics, we investigate the evolution toward onset of reconnection and the subsequent energy transfer and conversion. In either case, reconnection onset is preceded by a driven phase, during which magnetic flux is added to the tail at the high-latitude boundaries, followed by a relaxation phase, during which the configuration continues to respond to the driving. The boundary deformation leads to the formation of thin embedded current sheets, which are bifurcated in the near tail, converging to a single sheet farther out in the MHD simulations. The thin current sheets in the PIC simulation are carried by electrons and are associated with a strong perpendicular electrostatic field, which may provide a connection to parallel potentials and auroral arcs and an ionospheric signal even prior to the onset of reconnection. The PIC simulation very well satisfies integral entropy conservation (intrinsic to ideal MHD) during this phase, supporting ideal ballooning stability. Eventually, the current intensification leads to the onset of reconnection, the formation and ejection of a plasmoid, and a collapse of the inner tail. The earthward flow shows the characteristics of a dipolarization front: enhancement of B_z, associated with a thin vertical electron current sheet in the PIC simulation. Both MHD and PIC simulations show a dominance of energy conversion from incoming Poynting flux to outgoing enthalpy flux, resulting in heating of the inner tail. Localized Joule dissipation plays only a minor role.

1. Introduction

It is now well established that magnetic reconnection plays a crucial role in the energy release and transport associated with magnetospheric substorms. However, the onset of reconnection and its association with observed substorm onset signatures is less well understood. It is generally believed that the onset of reconnection involves a generalized tearing instability, where "generalized" means that the underlying configuration is not a plane one-dimensional current sheet, as assumed in the original tearing theory [*Furth et al.*, 1966], but contains variations along the sheet as well as a normal magnetic field component, which is characteristic of the magnetotail. The onset of tearing in two-dimensional magnetotail-like configurations is apparently no problem in resistive magnetohydrodynamic (MHD) models, as shown by linear theory [*Janicke*, 1980] and numerical resistive MHD simulations [*Birn*, 1980]. The MHD simulations also demonstrated that the magnetotail evolution following the imposed presence of resistivity, shows the major elements of the empirical reconnection substorm model [*McPherron et al.*, 1973; *Hones*, 1977]: formation of a near-Earth neutral line together with plasmoid formation and ejection. However, the source of resistivity and the applicability of the resistive model to the onset problem in the collisionless magnetotail plasma are questionable.

Schindler [1974] first concluded that the onset of collisionless tearing in a current sheet with finite normal magnetic field B_z requires a reduction of both the current sheet thickness and of B_z, and provided a quantitative onset criterion based on the existence of an ion-tearing instability. However, it was later shown that the ion-tearing mode becomes stabilized by electron compressibility effects for rather weak normal fields [*Pellat et al.*, 1991; *Brittnacher et al.*, 1995]. Nevertheless, the two parameters, normal magnetic field B_z and current sheet thickness, or equivalently current density magnitude, which are closely coupled [*Hesse and Birn*, 2000], remain the essential ingredients in the onset of tearing (or other current sheet instabilities). The onset problem thus becomes a problem of sufficient current sheet thinning, or of the formation of a thin embedded current sheet.

The formation of thin current sheets has been investigated by many authors. In application to the onset of reconnection associated with solar flares it was suggested that thin current sheets form within initially smooth configurations as the consequence of a slow evolution that leads to a critical state, at which neighboring smooth solutions cease to exist ("loss of equilibrium") [e.g., *Parker*, 1972, 1994; *Syrovatskii*, 1971, 1978; *Priest*, 1981; *Priest et al.*, 1995].

Thin current sheet formation from magnetotail convection was demonstrated through particle-in-cell (PIC) simulations by *Pritchett and Coroniti* [1994] in two-dimensional configurations with a uniform applied electric field and later by *Pritchett* [2005] in a three-dimensional simulation with an external electric field localized in the x direction, leading not only to the formation of a thin embedded current sheet but also to the onset of reconnection without involvement of significant cross-tail modes. *Pritchett* [2010] extended this approach to realistic ion/electron mass ratio within a two-dimensional PIC simulation and showed that the onset of reconnection, as well as the reconnection rate did not significantly depend on the assumed mass ratio.

In these simulations, the driving field was applied continuously. In contrast, *Birn et al.* [1994], through MHD simulations, and *Hesse et al.* [1996b], through hybrid particle simulations, demonstrated that a finite deformation of the magnetotail, equivalent to a temporally limited driving, could also lead to the formation of thin embedded current sheets. This concept was further proven theoretically for quasi-static evolution of two-dimensional equilibria [*Birn and Schindler*, 2002], based on mass and entropy conservation on closed magnetic flux tubes for magnetotail-like configurations. *Birn and Schindler* [2002] showed analytically that a finite boundary perturbation could lead to a loss of equilibrium, and that the limiting state was characterized by an embedded thin intense current sheet, which, in a 2-D configuration, bifurcates into two embedded sheets closer to Earth. Temporally limited driving was also the basis for a comparison study of the subsequent onset and growth of reconnection in a Harris current sheet, denoted as "forced" reconnection [*Birn et al.*, 2005].

A major assumption of this concept is the conservation of an entropy integral, defined for 2-D configurations by

$$S(A) = \int p^{1/\gamma} ds/B \tag{1}$$

where A is a flux variable with $B = \nabla A(x,z) \times \hat{\mathbf{y}}$, and the integration is taken along closed field lines from one boundary intersection to the other. In equilibrium, when the pressure p is constant along field lines, $S = p^{1/\gamma}V$, where V is the differential flux tube volume defined as

$$V(A) = \int ds/B \tag{2}$$

The quantity $S(A)$ is conserved in ideal MHD by assumption. However, in particle simulations that do not necessarily satisfy the ideal MHD approximations, the conservation of $S(A)$ is not a given, considering also that the pressure tensor may be anisotropic and includes both ion and electron contributions. Nevertheless, *Birn et al.* [2006] demonstrated for reconnection in an initially one-dimensional Harris current sheet that $S(A)$ is a very well-conserved quantity also in PIC simulations of localized reconnection before and even after reconnection. The concept of thin current sheet formation in a magnetotail configuration by finite boundary perturbations, and the subsequent onset of reconnection, was further demonstrated through 2-D PIC simulations [*Hesse and Birn*, 2000; *Hesse and Schindler*, 2001]. Our present investigation follows the approach of *Hesse and Schindler* [2001], albeit at higher spatial resolution, addressing also possible features of importance for the connection between the magnetotail and ground signatures.

The variation of the entropy integral (1) along the tail is also the crucial element governing ballooning/interchange instability [*Schindler and Birn*, 2004]. Simply stated, a typical two-dimensional magnetotail configuration should be (ideal MHD) ballooning stable if the entropy function increases monotonically downtail. The conservation of a monotonic entropy function $S(A)$ together with a monotonic variation of A along the tail therefore would ensure ballooning stability.

The importance of extending the investigation of the entropy conservation to two-dimensional magnetotail configuration lies in the fact that closed field lines (with both foot points at the near-Earth boundary) exist prior to the onset of reconnection and that during the preonset evolution, the magnetic field strength at

the equatorial crossing point decreases. As a consequence, ions can become demagnetized earlier than electrons, such that entropy conservation, based on the total or ion pressure, might become violated before electron demagnetization can initiate tearing instability. If this would lead to a change in the monotonicity of the entropy function, ballooning instability might be initiated prior to the onset of reconnection. The properties of the entropy function can be investigated with a 2-D code, even though the ballooning modes themselves cannot be modeled.

In addition to the investigation of the entropy conservation and other characteristics of the preonset evolution, we also explore characteristics of the earthward flow, specifically signatures of a "dipolarization front" [*Nakamura et al.*, 2002], and the energy conversion and transfer associated with reconnection in the tail. This latter topic has been investigated in 3-D MHD simulations [*Birn and Hesse*, 2005] and in localized PIC simulations [*Birn and Hesse*, 2010] but not in PIC simulations of more realistic magnetotail reconnection.

2. Overview of the Numerical Procedure

2.1. Initial State

The initial magnetic field configuration is a two-dimensional generalized Harris-type magnetotail equilibrium [*Schindler*, 1972; *Birn et al.*, 1975], identical to the one chosen by *Hesse and Schindler* [2001]. It is given by a flux function

$$A(x,z) = -L\,[\ln\cosh\zeta - \ln\hat{B}(x)], \quad \zeta = \hat{B}(x)z/L \tag{3}$$

with

$$\hat{B}(x) = [1 + bx/(Lq)]^{-q} \tag{4}$$

choosing parameters

$$L = 2, \qquad b = 0.05, \qquad q = 0.6 \tag{5}$$

We note that x is taken as the positive downtail, opposite to magnetospheric coordinates, while B_x is assumed positive for $z > 0$. Here and in the following, we use normalized quantities, based on standard units for the PIC simulation, which are given by B_0, the magnitude of the lobe magnetic field at the left boundary $x = 0$, the ion inertial length (or ion skin depth) $\lambda_i = c/\omega_{pi}$ with $\omega_{pi} = \sqrt{n_0 e^2/(\epsilon_0 m_i)}$, and a time unit $1/\omega_{ci}$, where $\omega_{ci} = eB_0/m_i$ is the ion-cyclotron frequency. The reference density n_0 is chosen as the difference between central plasma sheet and lobe densities at $x = 0$. This yields a characteristic speed $v_0 = \lambda_i\omega_{ci} = B_0/\sqrt{\mu_0 m_i n_0}$, equal to the Alfvén speed defined by B_0 and n_0, an electric field unit $E_0 = v_0 B_0$, pressure $p_0 = B_0^2/\mu_0$, and a magnetic flux unit $B_0\lambda_i$. In the MHD simulations B_0, L, and n_0 are independent arbitrary units.

The initial magnetic field components and the plasma pressure are then given by

$$B_x = -\partial A/\partial z = \hat{B}\tanh\zeta \tag{6}$$

$$B_z = \partial A/\partial x = -\frac{b}{1 + bx/(Lq)}(1 - \zeta\tanh\zeta) \tag{7}$$

$$p = \frac{\hat{p}(x)}{\cosh^2\zeta} + p_b \qquad \text{where} \quad \hat{p}(x) = \frac{\hat{B}^2(x)}{2} \tag{8}$$

The initial temperature is assumed uniform with a unit $kT_0 = m_i v_0^2$, such that the density is proportional to the pressure with $T = 1/2$ in dimensionless units. T and p represent the sums of ion and electron contributions. A uniform background (lobe) density $\rho_b = 0.1$ and a corresponding lobe pressure $p_b = 0.05$ are included to keep the Alfvén speed finite in the lobe regions.

The box size is given by $0 \le x \le 60$ and $|z| \le 10$, using symmetry around $z = 0$ for the MHD simulations.

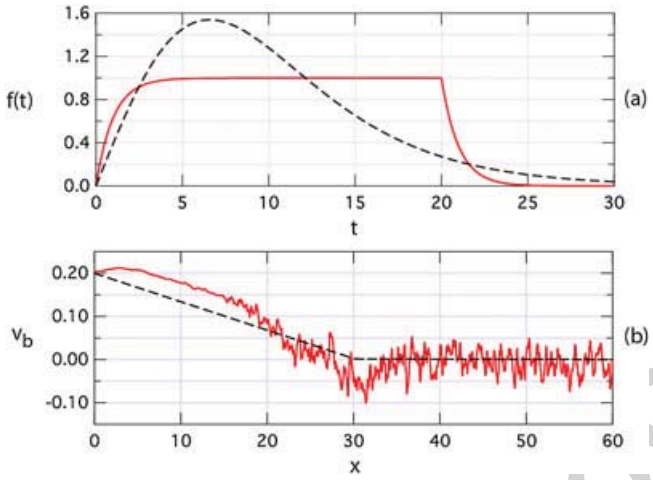

Figure 1. Inflow speed v_b in the PIC simulation at the top and bottom boundary, (a) as function of time, (b) as function of x at $t = 20$ (red solid lines). Black dashed lines show the inflow speed profiles applied in the MHD simulation, some of the simulations used an identical temporal profile as in the PIC simulation (red curve in Figure 1a).

2.2. Codes

The particle simulations are based on a 2.5-dimensional version of our fully electrodynamic particle-in-cell code [*Hesse and Schindler*, 2001], using 1600×800 grid cells in x, z with 2×10^8 particles of each species. Ions are assumed to be protons and a mass ratio $m_e/m_i = 1/100$ and initial temperature ratio $T_e/T_i = 1/5$ are used. The MHD simulations are based on an explicit leapfrog scheme [*Birn et al.*, 1996], using different grid resolutions with up to 240×240 cells to ensure that the reported results are not affected by the number of grid points.

Boundary conditions assume closed boundaries, except for the initial phase when the inflow of magnetic flux at the top and bottom are prescribed by an inflow speed v_z (MHD) or the corresponding electric field E_y (PIC). The left (near-Earth) boundary is also closed to inflow or outflow. However, the parallel flow speed v_z was also prescribed initially to be consistent with the inflow at the top and bottom boundaries.

3. Temporal Evolution

The evolution in both types of simulations is initiated by a perturbation at the boundary, consisting of a spatially and temporally limited inflow of magnetic flux, given by

$$v_{zb} = \pm v_b(x) f(t) \qquad \text{at } z = \mp 10 \tag{9}$$

The temporal and spatial profiles of the inflow speed v_z are shown in Figure 1 together with the spatial profile used in the MHD simulations (dashed line in Figure 1b). The inflow in the PIC simulation was forced by a boundary electric field $E_{yb} = v_{zb} B_x$, with v_{zb} given by (9), rather than the inflow speed. Due to the additional presence of a small tangential velocity component and the numerical implementation of the boundary inflow, the actual inflow speed v_z just inside of the boundary (red line in Figure 9b) did not have a smooth profile as function of x. F1

Two different temporal profiles were considered in the MHD simulations, one being identical to that of the PIC simulation, the other one, shown by the dashed line in Figure 1a, is given by

$$f(t) = 2a\omega \tanh \omega t / \cosh^2 \omega t \tag{10}$$

with parameters

$$a = 4 \qquad \omega = 0.1 \tag{11}$$

chosen to lead to an equivalent boundary deformation at $t = 20$. The two temporal profiles were found to cause no significant differences in the subsequent evolution. The main effects stemmed from the resulting boundary deformation, illustrated by a few selected field lines in Figure 2. Due to the fact that we keep the F2

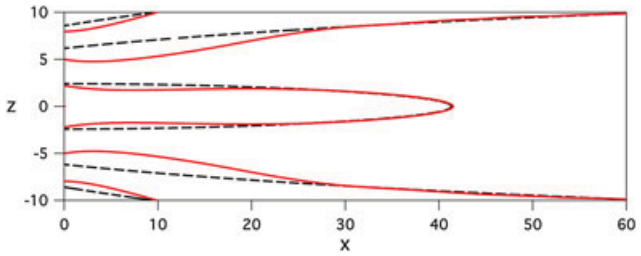

Figure 2. Field deformation by the boundary inflow, shown by a few selected field lines at $t = 0$ (dashed lines) and $t = 20$ (solid red lines).

inflow speed fixed over the driving period, the lobe magnetic field, and hence the electric field near the top and bottom, boundaries increase in time from ~ 0.2 to ~ 0.4 at $x = 0$ and from ~ 0.12 to ~ 0.16 at $x \approx 13$, which is the location of the X line formation.

The effects of the deformation, specifically current sheet thinning, continue even after the external driving subsides after $t = 20$. Reconnection onset in the PIC simulation does not occur until after $t = 60$, as demonstrated in Figure 3, which shows (top) the reconnected flux, defined by $\Psi_{rec} = \int B_z \, dx$ over the region where B_z is positive (in our coordinates), for the PIC simulation (solid red line) in comparison to three MHD simulations (blue lines), together with the evolution of (middle) the ion internal (thermal) energy and (bottom) the ion bulk kinetic energy. Figure 3, middle and bottom, demonstrate that the inflow of energy and magnetic flux causes a directly driven increase in ion thermal energy (and similarly electron thermal energy; not shown), but no significant change in the bulk kinetic energy. (The finite kinetic energy prior to the onset of reconnection stems from the ion flow speed associated with the equilibrium current.) F3

The early part of the PIC evolution might be considered as consistent with ideal MHD (apart from anisotropies, not included in ordinary MHD). For comparison, we therefore did not impose finite resistivity in the MHD simulations until after $t = 60$. In section 3.1 we focus on the evolution prior to the onset of reconnection, while the evolution after the onset of reconnection will be discussed in the subsequent sections.

3.1. Preonset Evolution, Thin Current Sheet Formation

Figure 4 shows the evolution of the cross-tail current density J_y during the early evolution prior to the onset of reconnection for (left) the PIC simulation and (right) the MHD simulation with $\eta = 0$. Obviously, the response to the boundary deformation is not finished at $t = 20$, although the inflow has subsided. Current F4

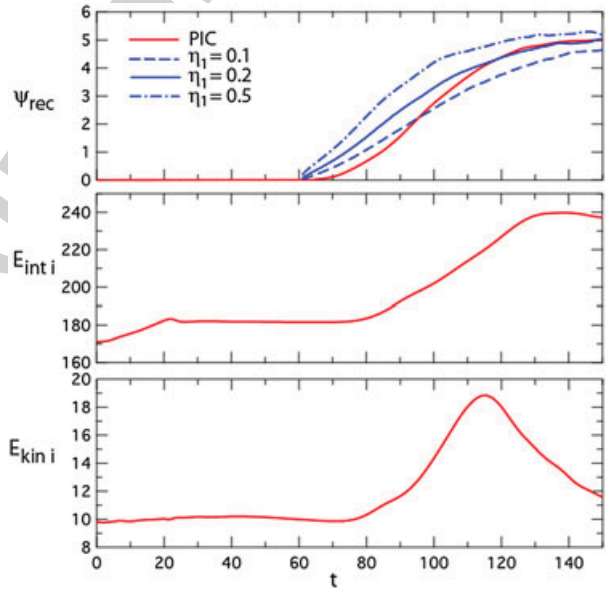

Figure 3. Evolution of (top) the reconnected flux for the PIC simulation (red solid line) and three MHD simulations with different values of the maximum resistivity η_1 (blue lines), (middle) ion internal energy, and (bottom) ion bulk kinetic energy.

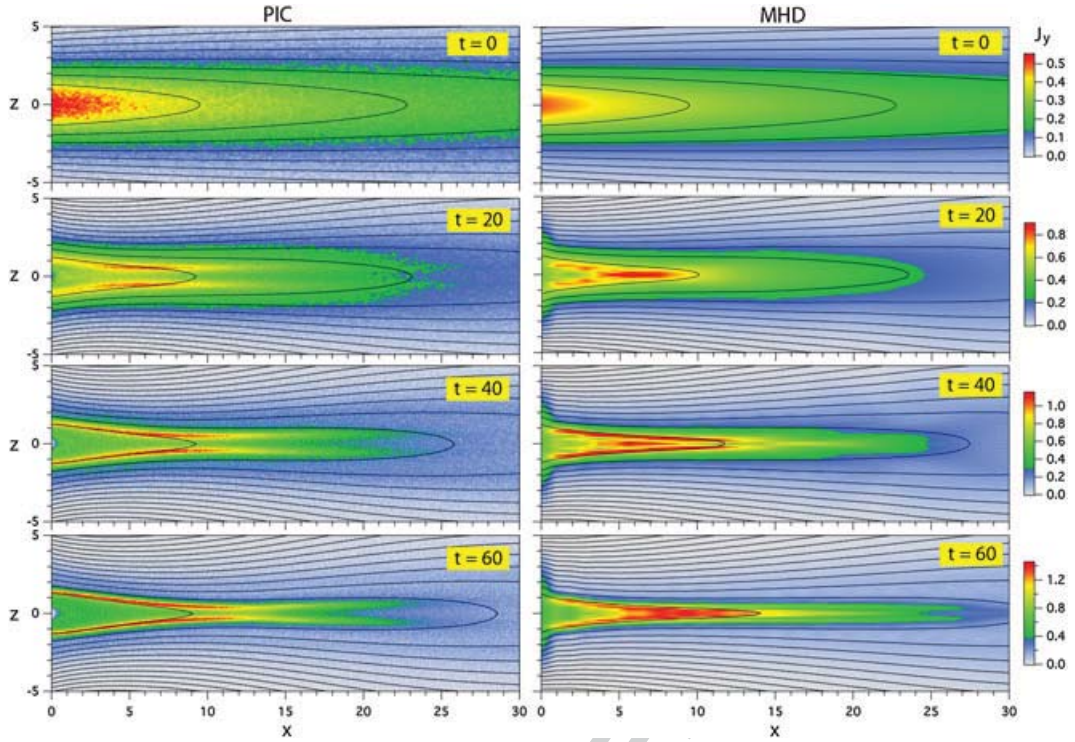

Figure 4. Evolution of the current density J_y during the preonset evolution: (left) PIC simulation and (right) ideal MHD simulation.

concentration and intensification continue. There is basic agreement in the development of bifurcated thin current sheets in the near tail. However, in contrast to the MHD simulation, in the PIC simulation, the bifurcated current sheets do not necessarily converge to a single sheet farther out. Possible reasons include time dependency and/or pressure anisotropy. The compression in z primarily increases the P_{zz} component, whereas the force balance in x is dominated by the P_{xx} component.

The bifurcated structure of the PIC current sheets by Figure 4 somewhat hides the fact that the current density also becomes enhanced in the center around $z = 0$ and that the overall thickness decreases substantially. This is demonstrated by Figure 5, which shows the current density profiles as functions of z for three different times at $x \approx 13.1$, which is close to the location where the neutral line starts to form. Solid lines correspond to the PIC simulation and dashed lines to the MHD simulation. The overall current concentration is similar in both PIC and MHD simulations; however, the internal structure differs. Similar substructures of the current sheet can also be found in PIC simulations of the slow compression of a one-dimensional current sheet [*Schindler and Hesse*, 2008, 2010]. However, the current concentration and the increase in the peak current density by a factor of ~3.5 in the 2-D case significantly exceed the values obtained in a 1-D compression.

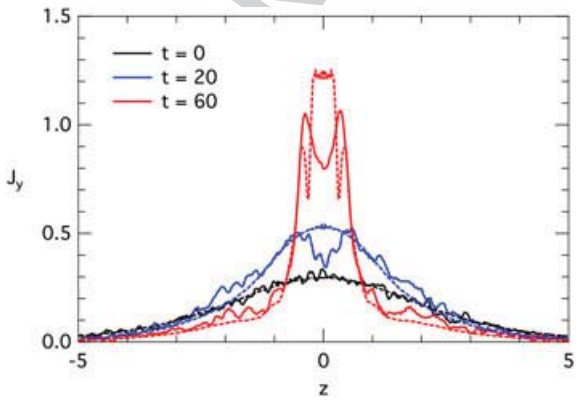

Figure 5. Current density as function of z at $x \approx 13$ for three different times. Solid lines correspond to the PIC simulation and dashed lines to the ideal MHD simulation.

Further insights into the effects of the external driving are given by Figure 6, showing the temporal evolution of the current sheet half-thickness L_h at the location $x \approx 13.1$ where the X line forms (top), defined as the distance from $z = 0$ to the location at which the current density decreases to 50% of its maximum value. The bottom part of Figure 6 shows the maximum current density. After onset, it is taken at or near the x location of the X line. Solid red

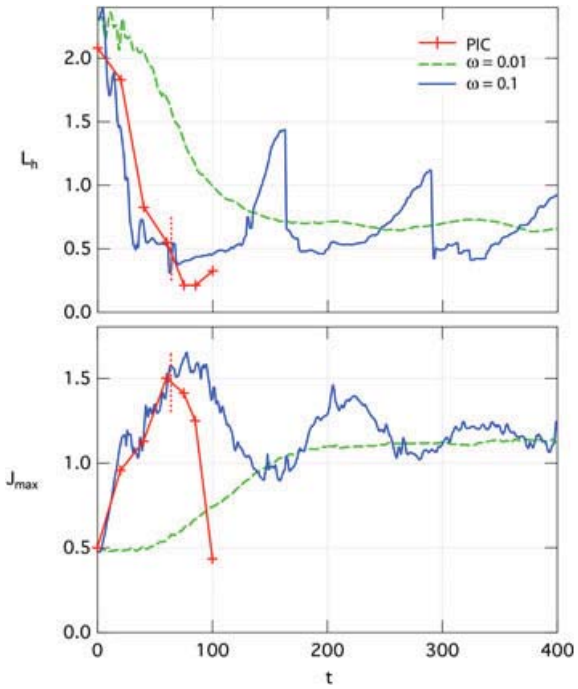

Figure 6. (Top) Current sheet (half-)thickness at $x \approx 13$ as function of time for PIC (solid red line) and two ideal MHD simulations (blue solid and green dashed lines); (bottom) maximum current density, taken at or near the location of the X line after X line formation, indicated by the red dotted lines.

lines represent the PIC simulation, red dotted lines indicated the time of X line formation. The green dashed and solid blue lines in Figure 6 represent two ideal MHD runs for different values of $\omega = 0.01$ and $\omega = 0.1$, respectively, as defined in equation (10), corresponding to different driving periods $1/\omega$. The two cases were designed to lead to the same final boundary perturbation.

The more slowly driven case ($\omega = 0.01$) can be considered as truly quasi-static: the configuration and the characteristic parameters L_h and J_{max} do not change significantly after the end of the driving period, $t > 200$. The more rapidly driven case $\omega = 0.1$, however, which is equivalent to the driving in the PIC simulation, although slow compared to a characteristic Alfvén period, causes oscillations in L_h and J_{max}, which eventually approach the values of the slowly driven case. The sudden jumps in L_h are caused by a temporary triple-peak structure of the current density as function of z. When the valleys surrounding the central peak are deep enough, L_h measures the half width of the central peak; otherwise, it measures the half width of the entire triple-peak structure. The slowly driven case does not exhibit such triple-peak structure. This might be taken as an indication that the double-peak structure of the current density in the PIC simulation prior to the onset of reconnection is also a time-dependent effect. Further simulations are necessary to resolve this issue.

The more rapid driving obviously leads to a more significant initial current density enhancement and current sheet thinning than the slow driving, easing the onset of reconnection. The current sheet half-thickness in the PIC simulation at the time of X line formation is ~ 0.5 ion skin depths (or ~ 5 electron skin depths for our mass ratio of $m_i/m_e = 100$),in agreement with the results of *Pritchett* [2010]. The thickness decreases further shortly after the neutral line formation, which was not shown by *Pritchett* [2010] but is consistent with observations [e.g., *Sanny et al.*, 1994]. The fact that the MHD simulations approach a minimum far in excess of the grid resolution is an indication that the evolution does not quite reach a critical state (corresponding to infinite local current density with $L_z \rightarrow 0$ in ideal MHD). However, the current sheet thinning is sufficient to initiate reconnection in the PIC simulation.

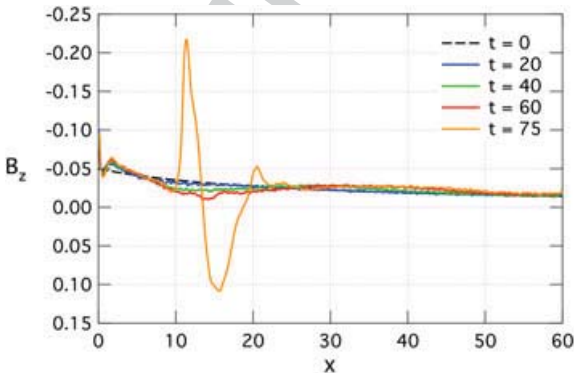

Figure 7. Normal magnetic field B_z in the PIC simulation at $z = 0$ as function of x for selected times prior to and shortly after the X line formation.

The variation of B_z along the x axis during the preonset evolution and shortly after onset is shown in Figure 7 for various selected times. It shows the reduction of B_z, which continues after the end of the driving period and assumes a minimum at $x \approx 14$, which later leads into the formation of an X line. The figure demonstrates the transition from a slow reduction of B_z during the relaxation phase ($t \leq 60$) to a rapid and drastic change after the onset ($t = 75$).

A topic of particular interest in the evolution prior to the onset of reconnection is the identification of signatures that might provide a connection to the ionosphere, specifically

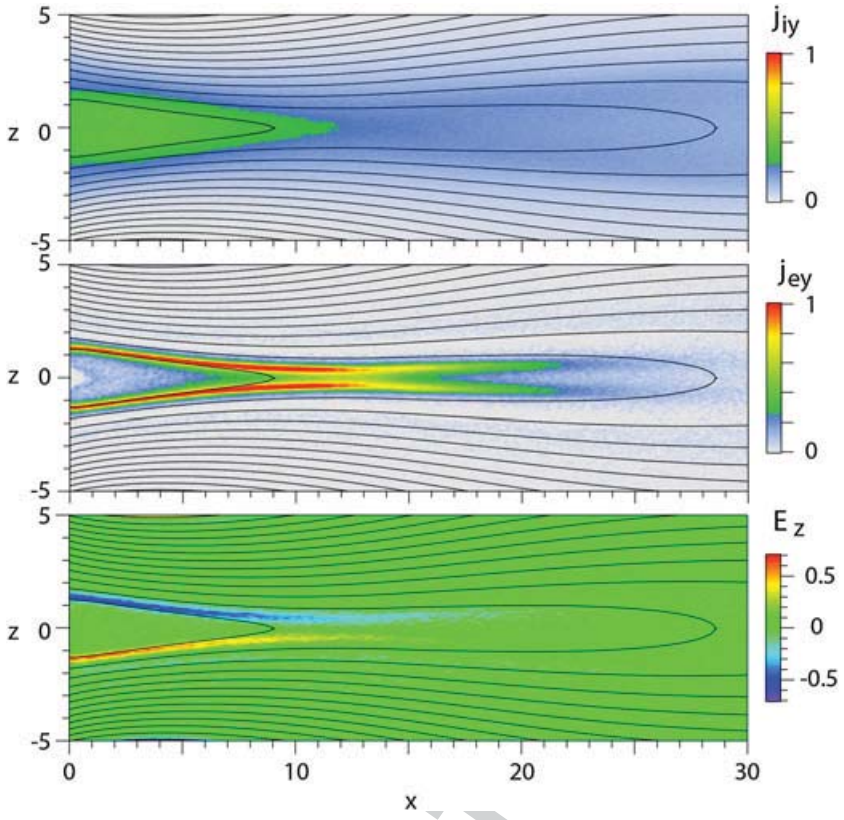

Figure 8. Current sheet structure in the PIC simulation at $t = 60$, corresponding to the left bottom panel of Figure 4: (top) ion current density, (middle) electron current density, and (bottom) electric field component E_z.

those that could be related to auroral arc formation or intensification, which is presumably the earliest near-Earth substorm onset identifier [*Akasofu*, 1964]. The possible connection between auroral arcs and thin current sheets in the magnetotail was pointed out by *Schindler and Birn* [2002], *Birn et al.* [2004], and *Birn et al.* [2012]. An important feature in thin electron current sheets that might be relevant for this connection is the electric field perpendicular to the current sheet, which is an intrinsic property of current sheets at small scales [e.g., *Pritchett and Coroniti*, 1994; *Hesse et al.*, 1996a]. Figure 8 shows the contribution of ion (top) and electron currents (middle) together with the electric field component E_z (bottom) at $t = 60$ in the PIC simulation, just before the onset of reconnection. It is quite obvious that the bifurcated current sheet, developed before the onset of reconnection, is carried by the electrons and has the characteristic signature of the perpendicular electric field, as pointed out already by *Birn et al.* [2012] for the time immediately after the formation of a neutral line. The associated potential drop is of the order of kT/e where $T = T_i + T_e$. Similar results were shown by *Pritchett* [2010] for the time after the onset of reconnection. F8

3.2. Postonset Evolution

The onset of reconnection occurs in the PIC simulation when the conditions are suitable for the onset of a tearing instability, particularly when B_z and the current sheet thickness are sufficiently reduced, at least locally, to demagnetize electrons, as indicated by Figures 6 and 7. The dissipation necessary for reconnection then is generated self-consistently. In the MHD simulation, numerical diffusion is not sufficient to initiate reconnection. As discussed above, we therefore imposed arbitrary localized resistivity after $t = 60$, given by

$$\eta = \eta_1 / \cosh^2\{[(x - x_0)/d_x^2 + (z/d_z)^2]\} \tag{12}$$

with $d_x = 2, d_z = 1$. The values of the peak resistivity η_1 were chosen to be close to unity (in normalized units), to approach reconnection rates commensurable with the rates in particle simulations [*Birn and Hesse*, 2001; *Otto*, 2001]. As shown by Figure 3, such agreement can indeed be achieved for $\eta_1 \approx 0.5$.

Figure 9 shows magnetic field lines and the plasma pressure of the PIC simulation (left) and the MHD simulation (right) in the x, z plane at different times. The times after the onset of reconnection were chosen to F9

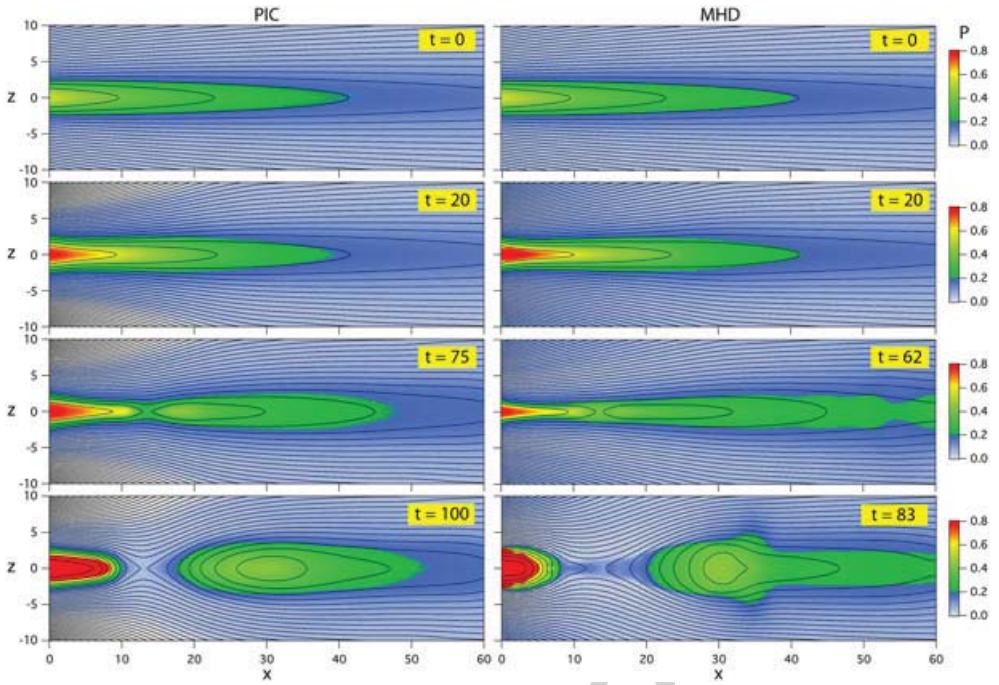

Figure 9. Evolution of the pressure and magnetic field: (left) PIC simulation and (right) MHD simulation with $\eta_1 = 0.5$. Times after onset are chosen to correspond to the same amount of reconnected flux; cf. Figure 3.

correspond to approximately equal amounts of reconnected flux in both simulations. The pressure in the PIC simulation is defined by one third of the trace of the full pressure tensor, given by the sum of ion and electron pressures. The overall evolution is very similar in both cases. The main difference is the fact that at the later stages the plasmoid magnetic island as well as the collapsing inner tail region becomes thicker in the MHD simulation.

4. Entropy

The flux tube entropy S, defined here by equation (1), has been identified as a major quantity governing not only preonset [*Birn and Schindler*, 2002] but also postonset evolution [*Birn et al.*, 2009; *Wolf et al.*, 2009; *Dubyagin et al.*, 2011]. Figure 10a shows $S(A)$ at different times during the PIC simulation. The pressure here is taken again as one third of the trace of the full pressure tensor (both ions and electrons), and the integral is taken from one boundary crossing at $x = 0$ to the other along closed field lines. To assure continuity, we added the northern and southern parts of $S(A)$ for field lines that were not closed within the simulation box, exiting through the distant boundary $x = 60$ or the top and bottom boundaries $|z| = 10$. The values A_3 and A_5 mark field lines that initially cross the corners of the simulation box at $x = 60, z = 0$, and $x = 60$, $|z| = 10$, respectively. F10

The function $S(A)$ remains unchanged during the compression phase, $t < 20$, and the subsequent relaxation phase prior to the onset of reconnection ($t < 60$, not shown). After the onset, at $t = 75$, plasmoid severance leads to a reduction of $S(A)$ between A_1, marking the first reconnected field line, and A_2. At later times, $t = 100$, reconnection and the reduction of $S(A)$ reach open field lines, indicated by proceeding to $A = A_4$. Figure 10a demonstrates not only the conservation of $S(A)$ prior to the onset and the localized reduction of $S(A)$ associated with the severance of a plasmoid but also the conservation of $S(A)$ on the shortened reconnected field lines after the onset.

The approximate conservation of $S(A)$ before and after reconnection holds not only for the full pressure but also for the individual contributions from ions and electrons, as demonstrated by Figure 10b for the electrons. This might indicate that both ions and electrons are heated fully adiabatically. However, closer inspection shows that there are deviations from the exact adiabatic behavior. If both ion and electron gases were compressed or expanded fully adiabatically, the pressure and temperature ratio would be exactly conserved. Figure 11 shows that the electron to ion pressure ratio remains conserved during the initial F11

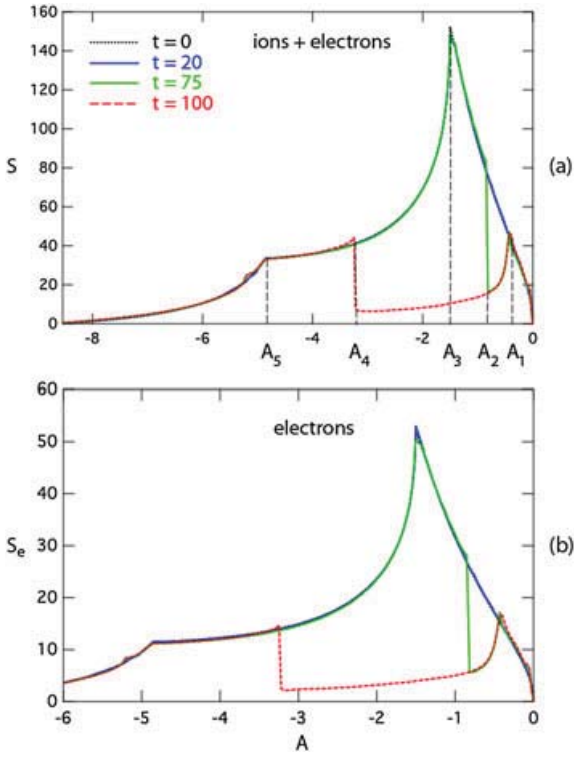

Figure 10. Entropy function $S(A)$, defined by equation (1), in the PIC simulation at different times: (a) for the sum of ion and electron pressures and (b) the same for the electrons only.

compression phase but increases by 10–20 % not only on reconnected field lines but also on the contracting field lines earthward of the reconnection site ($A > A_1$). In addition, there are anisotropy effects discussed in the following section.

5. Pressure Anisotropy

To further explore properties affecting the approximate conservation of $S(A)$, we have integrated the invariants of the double-adiabatic theory [*Chew et al.*, 1956]. Analogous to single-adiabatic theory, one can derive integral quantities by using mass conservation also. These quantities are given by

$$M_\perp(A) = \int \frac{p_\perp}{B}\frac{ds}{B} \tag{13}$$

and

$$M_\parallel(A) = \int p_\parallel^{1/3} B^{2/3}\frac{ds}{B} \tag{14}$$

Figure 12 shows $M_\perp(A)$ and $M_\parallel(A)$ at different times, demonstrating that both quantities are fairly well-conserved, apart from the losses through plasmoid severance. This holds despite the fact that the local double-adiabatic invariants are not necessarily conserved within a moving plasma element. The probable reason is that in double-adiabatic theory, heat flux is completely neglected, whereas the conservation of the field line integrals only requires negligible heat flux across field lines.

The conservation of the entropy function $S(A)$ and the double-adiabatic quantities $M_\perp(A)$ and $M_\parallel(A)$ does not result from the pressure remaining isotropic. Figure 13 demonstrates significant anisotropy, defined as $(p_\parallel - p_\perp)/p$, at three different times corresponding to the end of the driving phase ($t = 20$), just prior to the onset of reconnection ($t = 60$), and a late stage of energy and flux transfer ($t = 100$). The initial driving phase leads to an increase in perpendicular anisotropy, consistent with a dominance of betatron acceleration in the compressed lobe and outer plasma sheet fields. This anisotropy gets reduced significantly during the relaxation phase, possibly as a consequence of mirror instability, except near the plasma sheet boundary, where it increases due to the continued contraction. The isotropization, however, does not affect the conservation of the entropy integral (1). The later phase after the onset of reconnection leads to an increase in parallel anisotropy, consistent with first-order Fermi acceleration in the contracting near-Earth field and the ejected plasmoid.

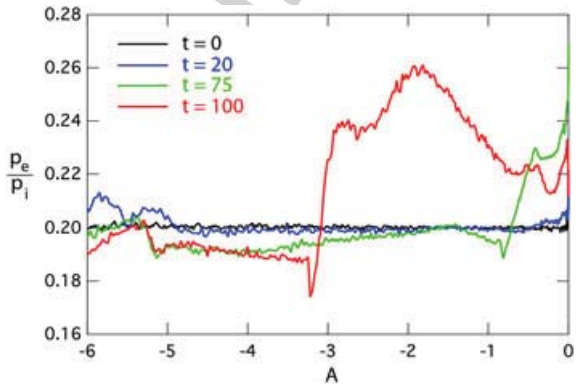

Figure 11. Ratio of electron to ion pressure in the PIC simulation, shown as function of A at four different times.

The plasma pressure is dominated by the ion pressure tensor. Further details of the ion pressure components as functions of A and t are shown in Figure 14. Since the pressure is not necessarily constant along field lines, the components P_{ii} are taken as field line averages. Figures 14a and 14b demonstrate that the initial compression primarily leads to an increase of P_{zzi}. However, due to approximate gyrotropy, $P_{yyi} \approx P_{zzi}$ close to the plasma sheet boundary $A \approx A_3$, whereas $P_{yyi} \approx P_{xxi}$ in the near tail where $A \approx 0$. This remains similar near or shortly after

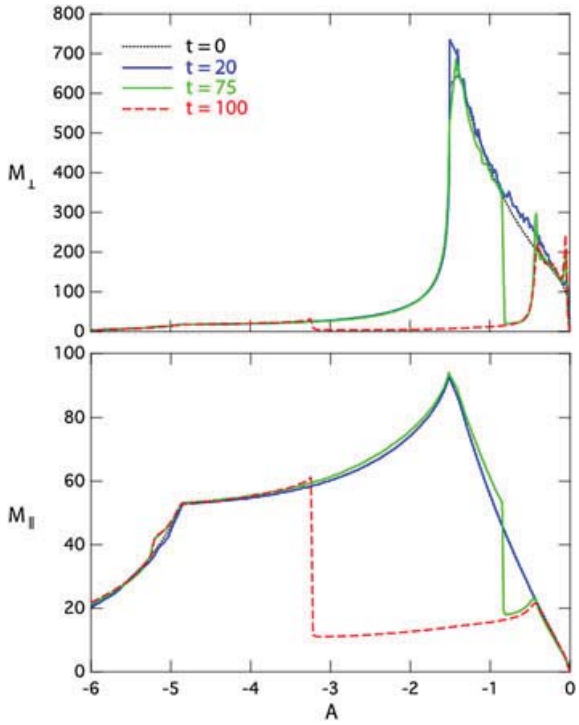

Figure 12. Invariants of double-adiabatic theory, integrated along field lines at different times: (top) $M_\perp(A) = \int (p_\perp/B)\mathrm{d}s/B$ and (bottom) $M_\parallel(A) = \int p_\parallel^{1/3} B^{2/3}\mathrm{d}s/B$.

the onset of reconnection (Figures 14b and 14c), whereas at later times (Figure 14d), the field collapse leads to a compression in x and a corresponding increase of P_{xxi}, while P_{yyi} and P_{zzi} approach each other, consistent with the parallel anisotropy shown in Figure 13. Figure 14b also demonstrates the steepening gradient of the pressure curves, which, in an isotropic equilibrium model, would be directly related to the current density increase ($J = \mathrm{d}p/\mathrm{d}A$). The electrons show a qualitatively similar behavior during the late phase, whereas they remain more closely isotropic in the earlier phases.

Despite the increase of the pressure on convecting field lines, local observations might show a decrease in pressure, as demonstrated by Figure 15 for both electron and ion pressure. Both decrease in the vicinity of the reconnection site due to the inflow of low-pressure field lines from the plasma sheet boundary layer and the lobes. The near-Earth part, however, shows an increase in pressure from the compression of closed field lines.

F15

6. Energy Transfer and Conversion

Using a one-fluid approximation and neglecting heat flux and pressure anisotropy, one can write energy conservation and conversion in the following form [e.g., *Birn and Hesse*, 2005]

$$\partial u_m/\partial t = -\nabla\cdot\mathbf{S} - \mathbf{j}\cdot\mathbf{E} = -\nabla\cdot\mathbf{S} - \mathbf{j}\cdot\mathbf{E}' - \mathbf{v}\cdot(\mathbf{j}\times\mathbf{B}) \quad (15)$$

$$\partial u_{\mathrm{th}}/\partial t = -\nabla\cdot\mathbf{H} + \mathbf{v}\cdot\nabla p + \mathbf{j}\cdot\mathbf{E}' \quad (16)$$

$$\partial u_k/\partial t = -\nabla\cdot\left(u_k\,\mathbf{v}\right) + \mathbf{v}\cdot(\mathbf{j}\times\mathbf{B} - \nabla p) \quad (17)$$

where $\mathbf{E}' = \mathbf{E} + \mathbf{v}\times\mathbf{B}$ is the electric field in the plasma rest frame, and

$$u_m = B^2/2 \quad (18)$$

$$u_{\mathrm{th}} = p/(\gamma - 1) \quad (19)$$

$$u_k = \rho v^2/2 \approx n m_i v_i^2/2 \quad (20)$$

represent magnetic, thermal, and bulk kinetic energy densities, respectively, with $\gamma = 5/3$ for an isotropic plasma pressure. The energy fluxes are defined by

$$\mathbf{S} = \mathbf{E}\times\mathbf{B} \quad \text{(Poynting vector)} \quad (21)$$

$$\mathbf{H} = (u_{\mathrm{th}} + p)\mathbf{v} \quad \text{(enthalpy flux)} \quad (22)$$

$$\mathbf{K} = u_k\mathbf{v} \quad \text{(bulk kinetic energy flux)} \quad (23)$$

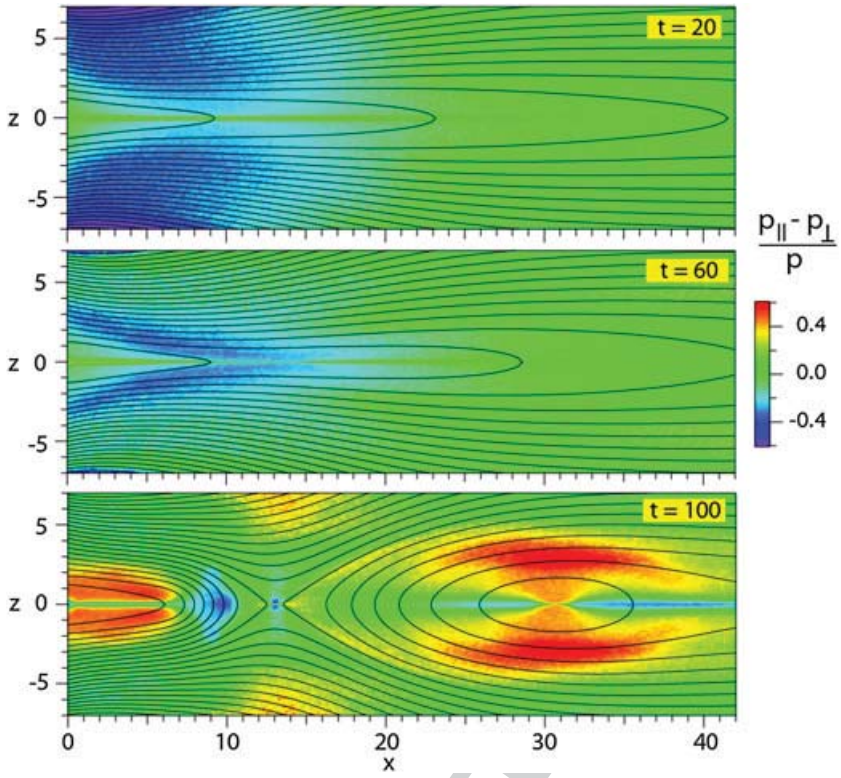

Figure 13. Pressure anisotropy $(p_{\parallel} - p_{\perp})/p$ in the PIC simulation at three different times.

Spatial details of the dominant ingoing and outgoing energy fluxes are shown in Figure 16, together with the (top) electric field component E_y, at the corresponding times $t = 85$ (PIC) and $t = 75$ (MHD). For better comparison between PIC and MHD results, we have evaluated the PIC energy fluxes also in a one-fluid manner, identifying p again with one third of the trace of the full pressure tensor and neglecting anisotropy contributions to $\mathbf{H}$. There are differences, primarily in magnitude, but generally good qualitative agreements

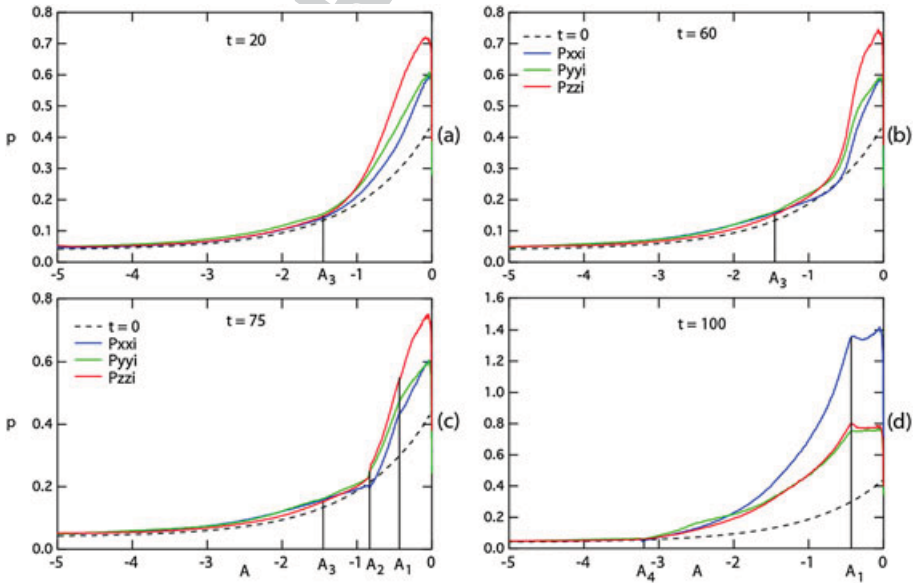

Figure 14. Average ion pressure components as function of the flux variable A at four different times. The meaning of the flux values A_1 – A_4 is the same as in Figure 10a: A_3 represents the open-closed boundary, before reconnection reaches open field lines, connected to $x = 60, z = 0$, A_1 represents the first reconnected field line, A_2 and A_4 represent separatrix field lines, reconnected at $t = 75$ and $t = 100$, respectively.

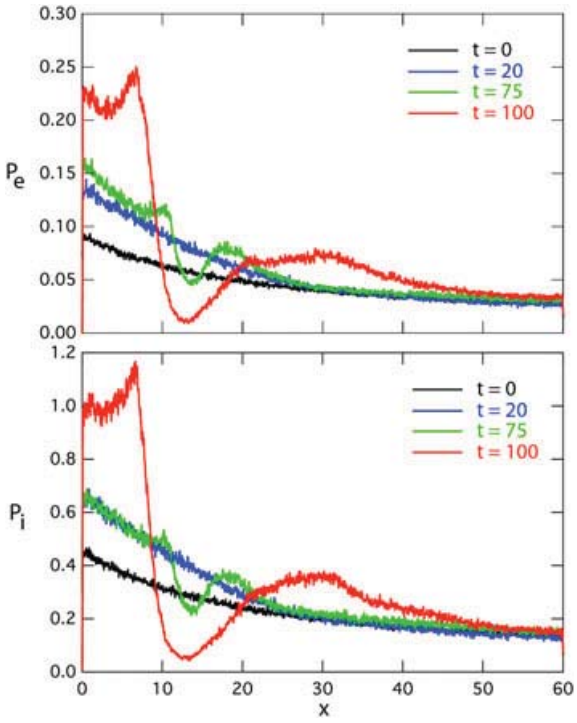

Figure 15. Electron and ion pressure along the x axis at four different times.

Figure 16, for two MHD simulation with $\eta_1 = 0.5$ (solid lines) and $\eta_1 = 0.2$ (dashed lines), together with three different instants in the PIC simulation (circles). Showing the fluxes as function of reconnected flux, Ψ_{rec}, rather than time, enables us to show both MHD runs together with the PIC results. Positive and negative values represent tailward and earthward fluxes, respectively. The enthalpy fluxes in the PIC simulation have been evaluated in two ways, with the isotropy approximation equation (22) and with the full anisotropic pressure tensor (shown in Figure 17). The differences are only of the order of a few percent.

The PIC and MHD simulations agree in the order of magnitude of the energy flows and in the fact that enthalpy flux is the dominant outflow in both directions, and that outgoing Poynting flux and bulk kinetic energy flux are smaller by about 1 order of magnitude (although their relative order is sometimes different between PIC and MHD). PIC and MHD also show a similar energy flow burst in the earthward direction for between PIC and MHD. The MHD flow and the associated enthalpy flux have advanced closer to the Earth at this time. The electric field in both simulations is relatively uniform only in a subsection of the box considered. This indicates that the box in consideration is not in full steady state. The MHD electric field is more enhanced at this time, but the extent and the location of the regions of enhanced E_y agree well, although they change in time for both types of simulations. The MHD simulation also shows an expansion in z (associated with a reversal of E_y and S_z) earthward and tailward of the reference box, not seen in the PIC simulation. It is noteworthy, however, that such an expansion, which may be part of a quasi periodic pulsation, has been found also in Thermal Emission Imaging System observations as consequences of earthward flow bursts and dipolarizations [*Panov et al.*, 2010].

The temporal variation of the outgoing energy fluxes from the reconnection site is shown in Figure 17, integrated over the boundaries of the box $8 < x < 20$, $|z| < 2.0$, shown in F17

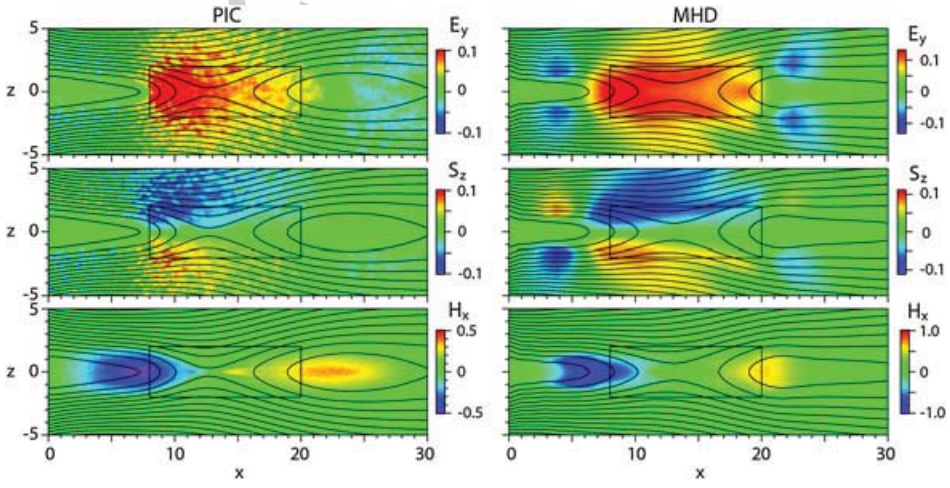

Figure 16. Electric field and dominant ingoing and outgoing energy fluxes, at (left) $t = 85$ for the PIC simulation and at (right) $t = 69$ for an MHD simulation with $\eta_1 = 0.5$: (top) electric field component E_y, (middle) ingoing Poynting flux S_z, and (bottom) outgoing enthalpy flux. The solid black rectangle shows the box used for the integrated fluxes shown in Figure 17.

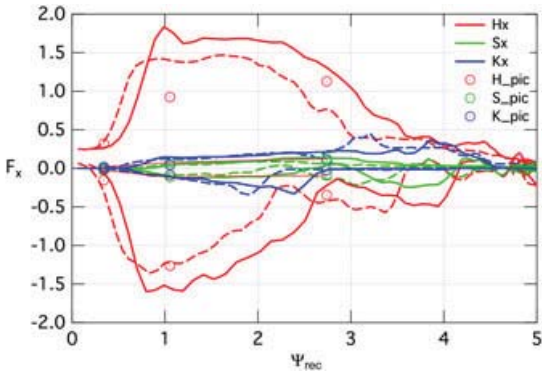

Figure 17. Outgoing energy fluxes from the reconnection site as function of reconnected magnetic flux. The energy fluxes are integrated over the boundaries of a box $8 < x < 20$, $|z| < 2.0$. Circles correspond to the PIC simulation, solid lines to an MHD simulation with $\eta_1 = 0.5$, and dashed lines to an MHD simulation with $\eta_1 = 0.2$. Positive and negative values represent tailward and earthward fluxes, respectively.

$\Psi_{rec} \approx 1$; however, the tailward energy flow shows a larger increase in the MHD simulation. We should stress, however, that the fluxes and the energy conversion are strongly time-dependent and that the PIC fluxes were evaluated only for three instants after the onset of reconnection.

The PIC fluxes shown in Figure 17 included both ions and electrons. Details of ion and electron contributions are given in Table 1 for $t = 85$ and $t = 100$, together with MHD results for $\eta_1 = 0.5$ at $t = 69$ and $t = 83$, respectively. The values in the table again show the relatively minor contributions of the outgoing Poynting and bulk kinetic energy fluxes. The outgoing fluxes typically exceed the incoming fluxes, in both PIC and MHD. This indicates again that the systems are not in a local steady state but that energy is released also from within the box considered. Table 1 also shows that the electron contributions to the outgoing enthalpy fluxes are more significant than estimates based on the original 1/5 electron to ion temperature ratio.

Figure 16 and Table 1 provide information of the instantaneous energy fluxes. A more global picture of the energy release and conversion can be obtained from considering the changes in energy densities, defined by equations (18)–(20). Figure 18 shows the changes of the energy densities between $t = 60$, just prior to the onset of reconnection, and $t = 100$. This time does not represent the final state, as can be seen from Figure 3. However, the later evolution is characterized by the plasmoid hitting the closed tailward boundary, causing reflections and oscillations, not applicable to the tail substorm evolution. Figure 18 indicates that the magnetic energy released from the lobes is converted primarily into thermal energy of the inner collapsed tail region. The thermal energy patterns for each species look very similar to Figure 18b, despite the fact that, at $t = 100$, 21.5% of the released energy has gone to electron heating, while 64.6% has gone into ion heating, more than expected from the initial temperature ratio of 1/5. The remainder of 13.9% has gone to bulk kinetic energy at this time, dominated by the ions.

Figure 18a also shows a reduction of the magnetic energy in the innermost portion of the tail, resulting from an expansion of the plasma sheet, as well as an increase near the equator around $x \approx 10$ and at higher latitudes, associated with the dipolarization. Figure 18b further shows a reduction of thermal energy density around the reconnection site. This results from the transport of plasma sheet plasma both earthward and tailward together with the inflow of lower pressure lobe plasma.

7. Dissipation and Dipolarization

Equations (15)–(17) show that the transfer of magnetic to thermal energy, via $\mathbf{j} \cdot \mathbf{E}$, may consist of a direct transfer via Joule dissipation $\mathbf{j} \cdot \mathbf{E}'$ (equivalent to Ohmic heating ηj^2 in MHD), which may be used to identify the "dissipation region" [*Zenitani et al.*, 2011], or, indirectly, of a transfer by Lorentz forces to bulk kinetic energy, $\mathbf{v} \cdot (\mathbf{j} \times \mathbf{B})$, with subsequent (or immediate) transfer to thermal energy, via $\mathbf{v} \cdot \nabla p$, resulting from

Table 1. Energy Fluxes Into and Out of the Box[a]

	S_{in}	S_{Earth}	S_{tail}	$H_{i,in}$	$H_{i,Earth}$	$H_{i,tail}$	$H_{e,in}$	$H_{e,Earth}$	$H_{e,tail}$	H_{in}	H_{Earth}	H_{tail}
PIC(85)	1.06	0.11	0.08	0.34	1.00	0.71	0.17	0.26	0.21	0.51	1.26	0.92
MHD(69)	1.52	0.09	0.03	-	-	-	-	-	-	0.83	1.52	1.83
PIC(100)	0.99	0.09	0.13	0.20	0.26	0.87	0.08	0.09	0.26	0.28	0.35	0.96
MHD(83)	1.11	0.01	0.14	-	-	-	-	-	-	0.48	0.31	1.38

[a]Indicated in Figure 16, taken at $t = 85$ and $t = 100$ for the PIC simulation, corresponding to $t = 69$ and $t = 83$, respectively, for the MHD simulation with $\eta_1 = 0.5$. Incoming fluxes are added over both top and bottom boundaries. The last three columns show the sum of ion and electron fluxes and the MHD enthalpy fluxes, respectively.

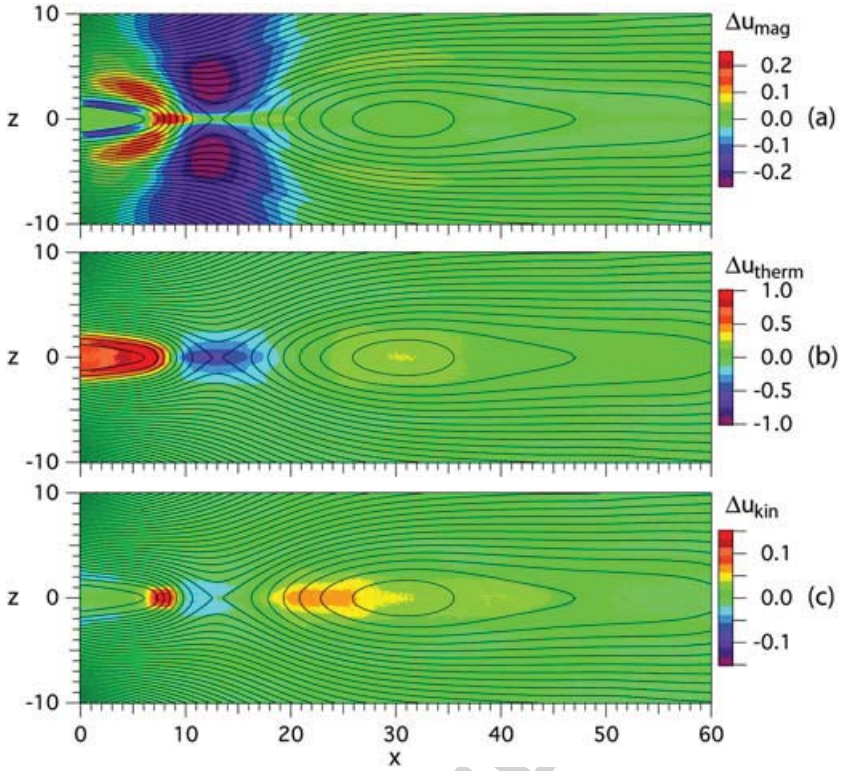

Figure 18. Changes in energy densities between $t = 60$ and $t = 100$, $\Delta u = u(100) - u(60)$, showing (a) magnetic energy, (b) thermal energy, and (c) bulk kinetic energy.

approximate force balance between Lorentz forces and pressure gradient forces [*Birn and Hesse*, 2005]. Figure 19 shows $\mathbf{j} \cdot \mathbf{E}'$ in the PIC simulation, together with the electron and ion contributions to $\mathbf{j} \cdot \mathbf{E}$ for two different times. The earlier time, $t = 85$, is close to the peak of the energy transfer into the earthward direction, as already shown in Figure 17, whereas at $t = 100$, the energy transfer to the tailward side dominates. The relative roles of ion and electron currents in the energy transfer $\mathbf{j} \cdot \mathbf{E}$, shown in the bottom two panels, as well as the earthward-tailward asymmetry, shown in the bottom panel are consistent with results of *Pritchett* [2010]. At both times, Joule heating, $\mathbf{j} \cdot \mathbf{E}'$, remains confined to the vicinity of the X line, dominated by the electron current contribution. Outside of that region, energy transfer takes place inside the separatrices within an earthward ($t = 85$) or tailward ($t = 100$) flow.

The earthward flow, which persists to $t = 100$, and the associated increase of B_z may be identified with a dipolarization front (DF) [*Nakamura et al.*, 2002], demonstrated earlier in 2-D and 3-D MHD simulations [*Hesse and Birn*, 1994; *Birn and Hesse*, 2000; *Birn et al.*, 2011] and 2-D hybrid simulations [*Hesse et al.*, 1998]

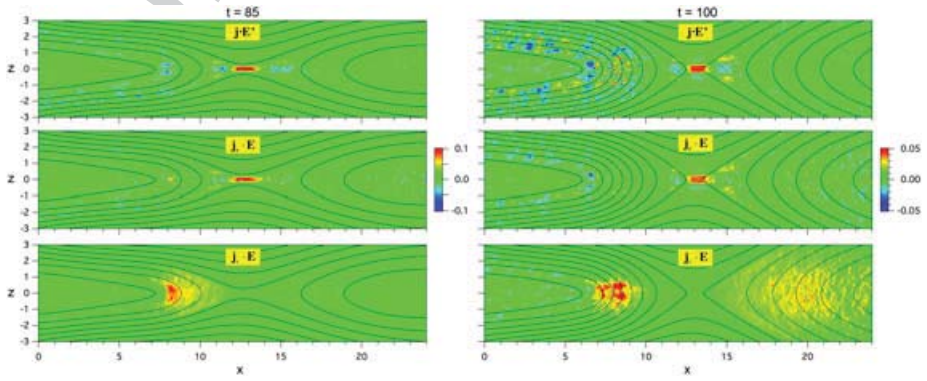

Figure 19. Joule dissipation $\mathbf{j} \cdot \mathbf{E}'$ and energy conversion $\mathbf{j}_e \cdot \mathbf{E}$, $\mathbf{j}_i \cdot \mathbf{E}$ from ion and electron currents in the PIC simulation at two different times.

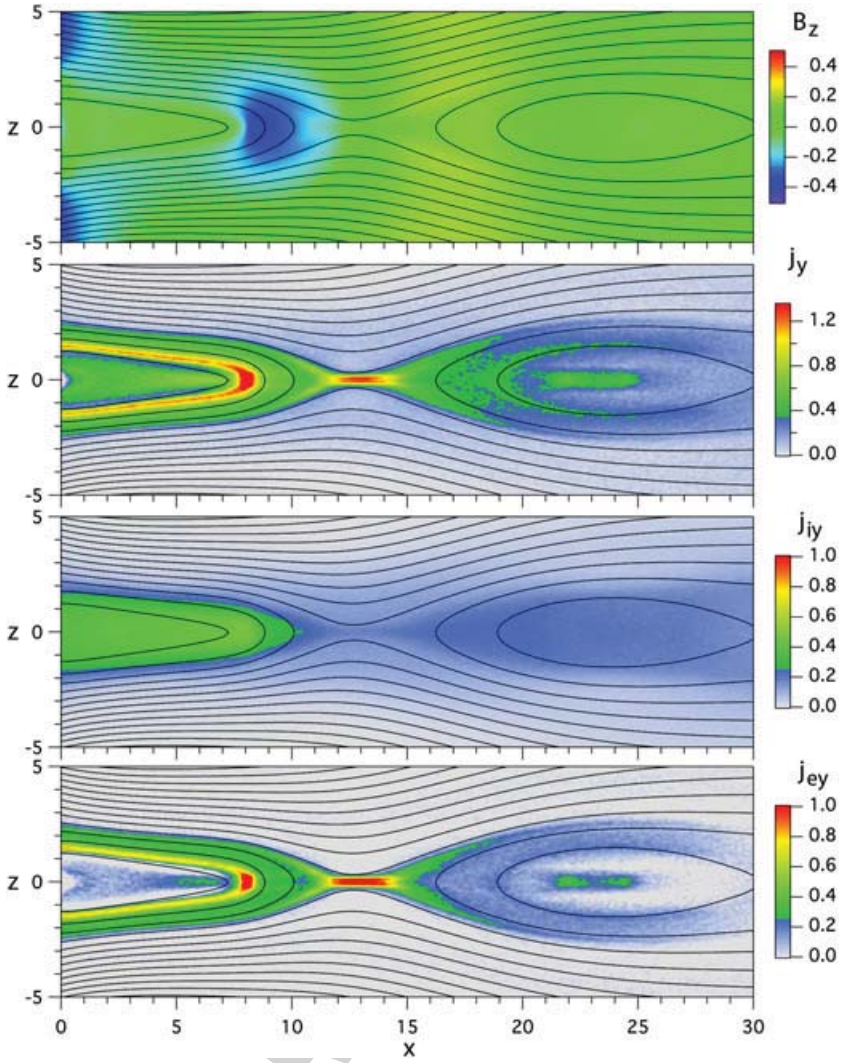

Figure 20. Magnetic field component B_z and cross-tail current density contributions in the PIC simulation at $t = 85$.

of magnetotail reconnection, as well as in more localized particle simulations of a reconnecting Harris sheet [*Sitnov et al.*, 2009].

Further details of the dipolarization front (DF) are given in Figures 20 and 21. Figure 20 shows the enhancement of B_z and the current contributions associated with the earthward flow, while Figure 21 shows the variation of B_z, E_x, and E_y along the x axis for three different times. It is obvious from Figure 20 that the sharp increase of the magnitude of B_z at the earthward edge is associated with an electron current, while the main cross-tail current earthward of the DF is carried by the ions (in the simulation frame). It is noteworthy that there is no equivalent sharp front on the tailward side. We further point out the sharp increase in the magnitude of E_x (our sign is opposite to that in GSM coordinates), which is comparable to or even exceeds the increase of E_y. This is a kinetic effect not included in MHD, resulting from the fact that the current in the thin vertical current sheet is a Hall current carried by $\mathbf{E} \times \mathbf{B}$ drift of the electrons. The x gradient of E_y decreases when the flow is slowed and magnetic flux is piled up at $t = 100$.

The absence of significant Joule dissipation at the DF, shown in Figure 19, indicates that the energy conversion in the DF is dominated by the ideal term $\mathbf{j} \cdot (-\mathbf{v} \times \mathbf{B}) = \mathbf{j} \cdot (-\mathbf{v}_e \times \mathbf{B})$. In agreement with *Sitnov et al.* [2009] and *Pritchett* [2010], we find that $\mathbf{j} \cdot \mathbf{E}$ at the DF is dominated by the ion current. This can be easily understood from the absence of significant dissipation $\mathbf{j} \cdot \mathbf{E}'$, which implies that $\mathbf{E} \approx -\mathbf{v}_e \times \mathbf{B}$, such that $\mathbf{j}_e \cdot \mathbf{E} \approx 0$ and

$$\mathbf{j}_i \cdot \mathbf{E} \approx ne\mathbf{v}_i \cdot (-\mathbf{v}_e \times \mathbf{B}) = \mathbf{v}_i \cdot (\mathbf{j}_e \times \mathbf{B}) \tag{24}$$

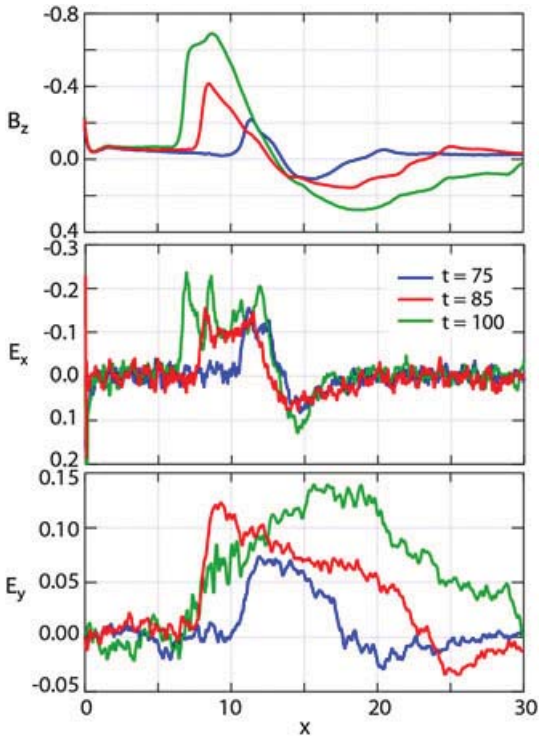

Figure 21. Variation of characteristic quantities in the PIC simulation along the x axis at three different times, (a) magnetic field component B_z, (b) electric field component E_x, and (c) electric field component E_y. To reduce noise, E_x is averaged in x and z over ± 5 neighboring grid points, while E_y is averaged over ± 2 neighboring points.

The energy conversion (we use the term "dissipation" in a narrower sense than *Sitnov et al.* [2009]) thus results from the ion acceleration by the Lorentz force associated with the dominant electron current (with subsequent thermalization). Observations of the presence or absence of Joule dissipation indicate variable results. A study of six dipolarization events by *Runov et al.* [2011] showed both positive and negative values for $\mathbf{j} \cdot \mathbf{E}'$ with an average positive.

8. Summary and Discussion

Using two-dimensional particle-in-cell and magnetohydrodynamic simulations of magnetotail dynamics, we have studied the onset of reconnection and the subsequent energy conversion and transfer. Specific emphasis of this investigation was on properties of the preonset phase and the energy transfer after onset in a realistic magnetotail scenario. In either simulation, reconnection onset was preceded by a driven phase, during which magnetic flux was added to the tail at the high-latitude boundaries, similar to the PIC simulation of *Hesse and Schindler* [2001] and three-dimensional MHD simulations [*Birn et al.*, 2011]. The inflow subsided after $t = 20$ (measured in ion-cyclotron periods). However, the configuration continued to adjust to the forced boundary deformation, and reconnection did not start in the PIC simulation until after $t = 60$. A comparison with ideal MHD simulations of similar boundary deformations but different time scales of the driving period indicates that this adjustment occurs on a characteristic time scale of ~ 100 Alfvén times. It is noteworthy that the continued adjustment to the change in boundary conditions does not lead to fast flows or noticeable increases in kinetic energy prior to the onset of reconnection.

For better comparison with the PIC simulation, the onset of reconnection in the resistive MHD simulation was initiated by imposing finite resistivity at $t = 60$. To approximate the fast growth in the PIC simulation, the resistivity was chosen to be spatially localized with a peak value corresponding to a Lundquist number (commonly also called magnetic Reynolds number) of order unity [e.g., *Birn and Hesse*, 2001; *Otto*, 2001].

The externally forced deformation leads to a current intensification and the formation of thin current sheets, which are bifurcated in the near tail, converging to a single embedded thin current sheet farther out in the MHD simulations. Eventually, the current concentration and intensification leads to the onset of reconnection (enforced in the MHD simulation by imposing finite resistivity), the formation and ejection of a plasmoid and a collapse of the inner tail. The onset time and the growth rate might be affected by the current bifurcation [*Camporeale and Lapenta*, 2005; *Matsui and Daughton*, 2008], which persisted close to onset, and the assumed mass ratio $m_i/m_e = 100$. However, these effects were not investigated in detail here.

The location of the X line is largely determined by the location of strongest thinning and reduction of B_z, which is about the same in PIC and MHD and the consequence of the applied boundary inflow. The relevant length scale for distance from the near-Earth boundary, therefore, is not a kinetic scale but the scale of the unperturbed plasma/current sheet, which is a few R_E in a realistic tail. Thus, the distance from the near-Earth boundary would be in the range 10–20 R_E, which seems realistic, considering also that our inner boundary is not the Earth.

Adiabatic ideal MHD theory and simulations [*Birn and Schindler*, 2002] have demonstrated that modest magnetotail deformations, satisfying mass, and entropy conservation on closed magnetic flux tubes, may lead to

thin current sheet formation and eventual loss of neighboring equilibrium, providing a plausible concept of the onset of instability and substorm initiation. The entropy conservation has been demonstrated previously in more localized PIC simulations of reconnection in a plane current sheet [*Birn et al.*, 2006; *Birn and Hesse*, 2010], but not in realistic magnetotail configurations. Here we demonstrated that prior to reconnection, and even after the plasmoid loss, the particle distributions satisfy very well integral entropy conservation, individually as well as one fluid, despite significant anisotropies.

However, the fact that the ideal MHD evolution leads to oscillations for more rapid driving ($\omega = 0.1$) and a gradual relaxation toward equilibrium values for slower driving ($\omega = 0.01$) (Figure 6) indicates that the system has not reached the threshold for loss of equilibrium, so that the onset of reconnection in the PIC simulation should be interpreted as an onset of (electron tearing) instability. This is supported by evaluating the electron gyrotropy parameter $\zeta = k\rho_n$ [*Hesse and Schindler*, 2001], where $k = 2\pi/\lambda$ and ρ_n is the electron gyro radius in the normal field B_n at $z = 0$. Using a characteristic wave length $\lambda \approx 10 d_i$ and a characteristic value of $B_n/B_0 \approx 0.02$ at $t = 60$, as indicated by Figure 6, we find $\zeta \approx \pi/2$. As discussed by *Hesse and Schindler* [2001], instability is expected when ζ approaches or exceeds a value close to unity.

The thin current sheets that develop during this phase in the PIC simulation are carried by electrons, consistent with earlier findings [*Pritchett and Coroniti*, 1994; *Hesse et al.*, 1996b], associated with a strong electrostatic perpendicular potential drop of the order of $k(T_i+T_e)/e$. The closure of the perpendicular potential through parallel electric fields may provide a near-Earth connection by driving auroral arcs even prior to the onset of reconnection [*Pritchett and Coroniti*, 1995; *Birn et al.*, 2004].

We further investigated the energy conversion and transfer. As in localized simulations of reconnection, Joule dissipation $\mathbf{j} \cdot \mathbf{E}'$, where $\mathbf{E}'$ is the electric field in the plasma rest frame, was found to be strongly localized and not significantly contributing to the energy conversion. The energy transfer mainly consists of a conversion of incoming Poynting flux to outgoing enthalpy flux, even to the open tail side. The PIC simulation and the MHD simulations agree in the basics and the approximate magnitude of the energy conversion, although not in all details. The PIC simulation shows a significant contribution of electrons to the overall energy budget, beyond what is expected from the initial 1/5 electron to ion temperature ratio.

The earthward flow in the PIC simulation also showed characteristics of a dipolarization front [*Nakamura et al.*, 2002], identified in MHD [*Hesse and Birn*, 1994; *Birn and Hesse*, 2000; *Birn et al.*, 2011], hybrid [*Hesse et al.*, 1998] and PIC simulations of magnetotail reconnection [*Pritchett*, 2010], as well as localized plane current sheet reconnection [*Sitnov et al.*, 2009]: a sharp enhancement of B_z associated with a thin vertical (i.e., y, z oriented) electron current sheet and a strong E_x component. Our simulation demonstrated the earthward propagation as well as a pileup of magnetic flux when the earthward propagation is stopped.

One important aspect of comparing PIC and MHD simulations is to find out to what extent particle simulation results can be approximated (or ignored) by fluid simulations. Here we focused on the evolution prior to the onset of reconnection and the energy conversion after reconnection. We found that the preonset evolution, including particularly the integral entropy conservation, is well described by ideal MHD, despite anisotropies and other kinetic effects in PIC simulations. Also, the energy conversion is qualitatively (within factors of ~2) in agreement. The onset time and mechanism are more problematic. Here we simply imposed resistivity values and onset times to agree roughly with the PIC results. It might be possible to identify onset times by characteristic values of the local magnetic field and current density, but it is not shown yet how well that works in general 3-D configurations. Also, the magnitude of resistivity applied here can provide maximum reconnection rates comparable to the fast rates of collisionless reconnection but the immediate imposition of high resistivity does not capture the more gradual onset of collisionless reconnection. More research is needed to resolve these issues.

Acknowledgments

Part of this work was performed at Los Alamos under the auspices of the US Department of Energy, supported by NSF grant GEM1203711 and NASA grants NNX13AD10G, NNX13AD21G, and NNX12AO98G.

Masaki Fujimoto thanks the reviewers for their assistance in evaluating this paper.

References

Akasofu, S.-I. (1964), The development of the auroral substorm, *Planet. Sci. Rev.*, *12*, 273–282, doi:10.1016/0032-0633(64)90151-5.

Birn, J. (1980), Computer studies of the dynamic evolution of the geomagnetic tail, *J. Geophys. Res.*, *85*, 1214–1222.

Birn, J., and M. Hesse (2000), The current disruption myth, in *Magnetospheric Current Systems, Geophys. Monogr. Ser.,* vol. 118, edited by S. Ohtani et al., p. 285, AGU, Washington, D. C.

Birn, J., and M. Hesse (2001), Geospace Environment Modeling (GEM) magnetic reconnection challenge: Resistive tearing, anisotropic pressure and Hall effects, *J. Geophys. Res.*, *106*, 3737–3750.

Birn, J., and M. Hesse (2005), Energy release and conversion by reconnection in the magnetotail, *Ann. Geophys.*, *23*, 3365–3373.

Birn, J., and M. Hesse (2010), Energy release and transfer in guide field reconnection, *Phys. Plasmas*, *17*, 012109.

Birn, J., and K. Schindler (2002), Thin current sheets in the magnetotail and the loss of equilibrium, *J. Geophys. Res.*, *107*(A7), SMP18, doi:10.1029/2001JA000291.
Birn, J., R. R. Sommer, and K. Schindler (1975), Open and closed magnetospheric tail configurations and their stability, *Astrophys. Space Sci.*, *35*, 389–402.
Birn, J., K. Schindler, and M. Hesse (1994), Magnetotail dynamics: MHD simulations of driven and spontaneous dynamic changes, in *Substorms-2, Proceedings of the Second International Conference on Substorms, Hamanako, Japan*, edited by J. R. Kan et al., p. 785, Univ. Alaska Fairbanks, Fairbanks, Alaska.
Birn, J., F. Iinoya, J. U. Brackbill, and M. Hesse (1996), A comparison of MHD simulations of magnetotail dynamics, *Geophys. Res. Lett.*, *23*, 323–326.
Birn, J., K. Schindler, and M. Hesse (2004), Thin electron current sheets and their relation to auroral potentials, *J. Geophys. Res.*, *109*, A02217, doi:1029/2003JA010303.
Birn, J., M. Hesse, and K. Schindler (2006), Entropy conservation in simulations of magnetic reconnection, *Phys. Plasmas*, *13*, 092117.
Birn, J., M. Hesse, K. Schindler, and S. Zaharia (2009), Role of entropy in magnetotail dynamics, *J. Geophys. Res.*, *114*, A00D03, doi:10.1029/2008JA014015.
Birn, J., R. Nakamura, E. Panov, and M. Hesse (2011), Bursty bulk flows and dipolarization in MHD simulations of magnetotail reconnection, *J. Geophys. Res.*, *116*, A01210, doi:10.1029/2010JA016083.
Birn, J., K. Schindler, and M. Hesse (2012), Magnetotail aurora connection: The role of thin current sheets, in *Auroral Phenomenology and Magnetospheric Processes: Earth and Other Planets, Geophys. Monogr. Ser.,* vol. 197, edited by A. Keiling et al., pp. 337–346, AGU, Washington, D. C. doi:10.1029/2011GM001182.
Birn, J., et al. (2005), Forced magnetic reconnection, *Geophys. Res. Lett.*, *32*, L06105, doi:10.1029/2004GL022058.
Brittnacher, M., K. B. Quest, and H. Karimabadi (1995), A new approach to the linear theory of single-species tearing in two-dimensional quasi-neutral sheets, *J. Geophys. Res.*, *100*, 3551–3562.
Camporeale, E., and G. Lapenta (2005), Model of bifurcated current sheets in the Earth's magnetotail: Equilibrium and stability, *J. Geophys. Res.*, *110*, A07206, doi:10.1029/2004JA010779.
Chew, G. F., M. L. Goldberger, and F. E. Low (1956), The Boltzmann equation and the one-fluid hydromagnetic equations in the absence of particle collisions, *Proc. R. Soc. London*, *236*(1204), 112–118.
Dubyagin, S., V. Sergeev, S. Apatenkov, V. Angelopoulos, A. Runov, R. Nakamura, W. Baumjohann, J. McFadden, and D. Larson (2011), Can flow bursts penetrate into the inner magnetosphere?, *Geophys. Res. Lett.*, *38*, L08102, doi:10.1029/2011GL047016.
Furth, H. P., J. Killeen, and M. Rosenbluth (1966), Finite resistivity instabilities of a sheet pinch, *Phys. Fluids*, *6*, 459–484.
Hesse, M., and J. Birn (1994), MHD modeling of magnetotail instability for localized resistivity, *J. Geophys. Res.*, *99*, 8565–8576.
Hesse, M., and J. Birn (2000), Near- and mid-tail current flow during substorms: Small-scale and large-scale aspects of current disruption, in *Magnetospheric Current Systems, Geophys. Monogr. Ser.,* vol. 118, edited by S. Ohtani et al., p. 295, AGU, Washington, D. C.
Hesse, M., and K. Schindler (2001), The onset of magnetic reconnection in the magnetotail, *Earth Planets Space*, *53*, 645–653.
Hesse, M., D. Winske, and M. Kuznetsova (1996a), Hybrid modeling of the formation and structure of thin current sheets in the magnetotail, in *Third International Conference on Substorms (ICS-3), ESA Publ. SP-389*, edited by E. J. Rolfe and B. Kaldeich, p. 231, European Space Agency.
Hesse, M., D. Winske, M. Kuznetsova, J. Birn, and K. Schindler (1996b), Hybrid modeling of the formation of thin current sheets in magnetotail configurations, *J. Geomagn. Geoelec.*, *48*, 749–763.
Hesse, M., J. Birn, and D. Winske (1998), Formation and structure of thin current sheets in the magnetotail: Dipolarization, in *Substorms-4*, edited by S. Kokubun, and Y. Kamide, p. 727, Terra Scientific Publishing Co./ Kluwer Academic Publishers, Dordrecht, Holland.
Hones, E. W., Jr (1977), Substorm processes in the magnetotail: Comments on 'On hot tenuous plasma fireballs and boundary layers in the Earth's magnetotail' by L. A. Frank, L. L. Ackerson, and R. P. Lepping, *J. Geophys. Res.*, *82*, 5633–5640.
Janicke, L. (1980), The resistive tearing mode in weakly two-dimensional neutral sheets, *Phys. Fluids*, *23*, 1843–1849.
Matsui, T., and W. Daughton (2008), Kinetic theory and simulation of collisionless tearing in bifurcated current sheets, *Phys. Plasmas*, *15*, 012901.
McPherron, R. L., C. T. Russell, and M. A. Aubry (1973), Satellite studies of magnetospheric substorms on August 15, 1968, 9, phenomenological model for substorms, *J. Geophys. Res.*, *78*, 3131–3149.
Nakamura, R., et al. (2002), Motion of the dipolarization front during a flow burst event observed by Cluster, *Geophys. Res. Lett.*, *29*(20), 1942, doi:10.1029/2002GL015763.
Otto, A. (2001), Geospace Environment Modeling (GEM) magnetic reconnection challenge: MHD and Hall MHD - constant and current dependent resistivity models, *J. Geophys. Res.*, *106*, 3751–3757.
Panov, E. V., et al. (2010), Plasma sheet thickness during a bursty bulk flow reversal, *J. Geophys. Res.*, *115*, A05213, doi:10.1029/2009JA014743.
Parker, E. N. (1972), Topological dissipation and the small-scale fields in turbulent gases, *Astrophys. J.*, *174*, 499–510.
Parker, E. N. (1994), *Spontaneous Current Sheets in Magnetic Fields*, Oxford Univ. Press, New York, NY.
Pellat, R., F. V. Coroniti, and P. L. Pritchett (1991), Does ion tearing exist?, *Geophys. Res. Lett.*, *18*, 143–146.
Priest, E. R. (1981), Current sheets, in *Solar Flare Magnetohydrodynamics*, edited by E. R. Priest, p. 139, Gordon and Breach, Newark, N. J.
Priest, E. R., V. S. Titov, and G. Rickard (1995), The formation of magnetic singularities by time-dependent collapse of an x-type magnetic field, *Philos. Trans. R. Soc. London A*, *351*, 1–37.
Pritchett, P. L. (2005), Externally driven magnetic reconnection in the presence of a normal magnetic field, *J. Geophys. Res.*, *110*, A05209, doi:10.1029/2004JA010948.
Pritchett, P. L. (2010), Onset of magnetic reconnection in the presence of a normal magnetic field: Realistic ion to electron mass ratio, *J. Geophys. Res.*, *115*, A10208, doi:10.1029/2010JA015371.
Pritchett, P. L., and F. V. Coroniti (1994), Convection and the formation of thin current sheets in the near-Earth plasma sheet, *Geophys. Res. Lett.*, *21*(15), 1587–1590, doi:10.1029/94GL01364.
Pritchett, P. L., and F. V. Coroniti (1995), Formation of thin current sheets during plasma sheet convection, *J. Geophys. Res.*, *100*(A12), 23,551–23,565, doi:10.1029/95JA02540.
Runov, A., V. Angelopoulos, X.-Z. Zhou, X.-J. Zhang, S. Li, F. Plaschke, and J. Bonnell (2011), A THEMIS multicase study of dipolarization fronts in the magnetotail plasma sheet, *J. Geophys. Res.*, *116*, A05216, doi:10.1029/2010JA016316.
Sanny, J., R. L. McPherron, C. T. Russell, D. N. Baker, T. I. Pulkkinen, and A. Nishida (1994), Growth-phase thinning of the near-Earth current sheet during the CDAW 6 substorm, *J. Geophys. Res.*, *99*, 5805–5816.
Schindler, K. (1972), A self-consistent theory of the tail of the magnetosphere, in *Earth's Magnetospheric Processes*, edited by B. M. McCormac, p. 200, D. Reidel, Norwell, Mass.

Schindler, K. (1974), A theory of the substorm mechanism, *J. Geophys. Res.*, *79*, 2803–2810.
Schindler, K., and J. Birn (2004), MHD stability of magnetotail equilibria including a background pressure, *J. Geophys. Res.*, *109*, A10208, doi:10.1029/2004JA010537.
Schindler, K., and J. Birn (2002), Models of two-dimensional embedded thin current sheets from Vlasov theory, *J. Geophys. Res.*, *107*(A8), SMP20, doi:10.1029/2001JA000304.
Schindler, K., and M. Hesse (2008), Formation of thin bifurcated current sheets by quasisteady compression, *Phys. Plasmas*, *15*, 042902.
Schindler, K., and M. Hesse (2010), Conditions for the formation of nongyrotropic current sheets in slowly evolving plasmas, *Phys. Plasmas*, *17*, 082103.
Sitnov, M. I., M. Swisdak, and A. V. Divin (2009), Dipolarization fronts as a signature of transient reconnection in the magnetotail, *J. Geophys. Res.*, *114*, A04202, doi:10.1029/2008JA013980.
Syrovatskii, S. I. (1971), Formation of current sheets in a plasma with a frozen-in strong magnetic field, *Sov. Phys. JETP*, *33*, 933–940.
Syrovatskii, S. I. (1978), On the time evolution of force-free fields, *Sol. Phys.*, *58*, 89–94.
Wolf, R. A., Y. Wan, X. Xing, J.-C. Zhang, and S. Sazykin (2009), Entropy and plasma sheet transport, *J. Geophys. Res.*, *114*, A00D05, doi:10.1029/2009JA014044.
Zenitani, S., M. Hesse, A. Klimas, and M. Kuznetsova (2011), New measure of the dissipation region in collisionless magnetic reconnection, *Phys. Rev. Lett.*, *106*, 195003, doi:10.1103/PhysRevLett.106.195003.

Author Query Form

Journal: Journal of Geophysical Research: Space Physics

Article: jgra_50791

Dear Author,

During the copyediting of your paper, the following queries arose. Please respond to these by annotating your proofs with the necessary changes/additions.

- If you intend to annotate your proof electronically, please refer to the E-annotation guidelines.
- If you intend to annotate your proof by means of hard-copy mark-up, please refer to the proof mark-up symbols guidelines. If manually writing corrections on your proof and returning it by fax, do not write too close to the edge of the paper. Please remember that illegible mark-ups may delay publication.

Whether you opt for hard-copy or electronic annotation of your proofs, we recommend that you provide additional clarification of answers to queries by entering your answers on the query sheet, in addition to the text mark-up.

Query No.	Query	Remark
Q1	AUTHOR: Please check if author affiliations are provided correctly.	
Q2	AUTHOR: The subscript "earth" in Table 1 has been changed to "Earth". Please check and change if correct.	
Q3	AUTHOR: Please provide the city location of publisher for Reference “Hesse et al. 1996a”.	

PUBLICATION FEE CONSENT FORM

Dear Author:

As documented on the Steps to Publications webpage, content accepted for publication in an AGU journal may be subject to publication fees. The current fee schedule for AGU journals is available from the Author Resources webpage.

This consent form has been generated for you in accordance with this policy on the basis of the final word, table, and figure counts of your article. The word count is for the abstract, body text, and captions only. Please review the calculated publication fee below, complete any relevant fields necessary for us to process your final invoice, and return a signed copy of this form to the production editor with your proof corrections. A final invoice will be mailed to the named billing contact within a few weeks of your articles appearance online in edited format.

Please note: OnlineOpen, the open access option for AGU journals, must be purchased through the OnlineOpen order form (https://authorservices.wiley.com/bauthor/onlineopen_order.asp). If you elected OnlineOpen at any earlier phase of submission and have not already submitted your order online, please do so now. Authors who select OnlineOpen will not be charged any base publication fee, but excess length fees will still apply.

ARTICLE DETAILS

Journal: Journal of Geophysical Research: Space Physics

Article: Birn, J., and M. Hesse (2014), Forced reconnection in the near magnetotail: Onset and energy conversion in PIC and MHD simulations, J. Geophys. Res. Space Physics, 119, 1–20, doi:10.1002/2013JA019354.

Words: 6,661
Figures: 21
Tables: 1
OnlineOpen: No

Publishing Units: 35
Excess Publishing Units: 10
Publication Fee: USD $ 2250

BILLING DETAILS

Name: _____ **Phone:** _____
Address: _____ **E-mail:** _____
_____
_____

Signature: _____ **Date:** _____

WILEY-BLACKWELL

USING e-ANNOTATION TOOLS FOR ELECTRONIC PROOF CORRECTION

Required software to e-Annotate PDFs: Adobe Acrobat Professional or Adobe Reader (version 7.0 or above). (Note that this document uses screenshots from Adobe Reader X)
The latest version of Acrobat Reader can be downloaded for free at: http://get.adobe.com/uk/reader/

Once you have Acrobat Reader open on your computer, click on the Comment tab at the right of the toolbar:

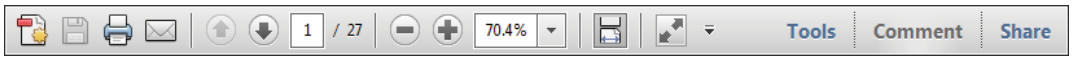

This will open up a panel down the right side of the document. The majority of tools you will use for annotating your proof will be in the Annotations section, pictured opposite. We've picked out some of these tools below:

1. Replace (Ins) Tool – for replacing text.

Strikes a line through text and opens up a text box where replacement text can be entered.

How to use it

- Highlight a word or sentence.
- Click on the Replace (Ins) icon in the Annotations section.
- Type the replacement text into the blue box that appears.

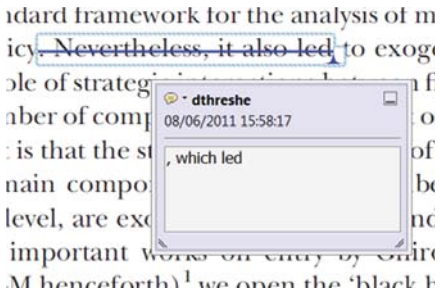

2. Strikethrough (Del) Tool – for deleting text.

Strikes a red line through text that is to be deleted.

How to use it

- Highlight a word or sentence.
- Click on the Strikethrough (Del) icon in the Annotations section.

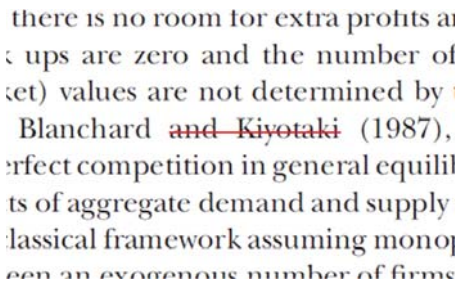

3. Add note to text Tool – for highlighting a section to be changed to bold or italic.

Highlights text in yellow and opens up a text box where comments can be entered.

How to use it

- Highlight the relevant section of text.
- Click on the Add note to text icon in the Annotations section.
- Type instruction on what should be changed regarding the text into the yellow box that appears.

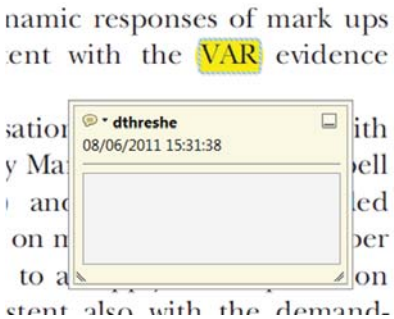

4. Add sticky note Tool – for making notes at specific points in the text.

Marks a point in the proof where a comment needs to be highlighted.

How to use it

- Click on the Add sticky note icon in the Annotations section.
- Click at the point in the proof where the comment should be inserted.
- Type the comment into the yellow box that appears.

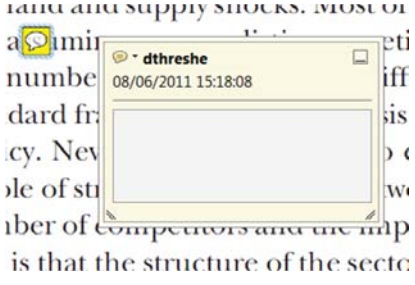

USING e-ANNOTATION TOOLS FOR ELECTRONIC PROOF CORRECTION

5. Attach File Tool – for inserting large amounts of text or replacement figures.

Inserts an icon linking to the attached file in the appropriate pace in the text.

How to use it

- Click on the Attach File icon in the Annotations section.
- Click on the proof to where you'd like the attached file to be linked.
- Select the file to be attached from your computer or network.
- Select the colour and type of icon that will appear in the proof. Click OK.

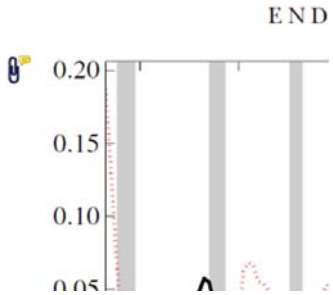

6. Add stamp Tool – for approving a proof if no corrections are required.

Inserts a selected stamp onto an appropriate place in the proof.

How to use it

- Click on the Add stamp icon in the Annotations section.
- Select the stamp you want to use. (The Approved stamp is usually available directly in the menu that appears).
- Click on the proof where you'd like the stamp to appear. (Where a proof is to be approved as it is, this would normally be on the first page).

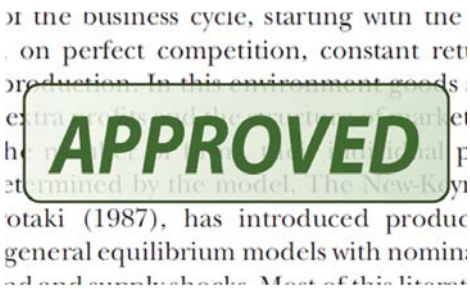

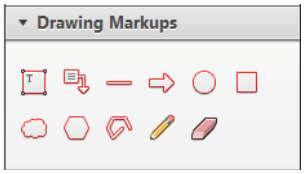

7. Drawing Markups Tools – for drawing shapes, lines and freeform annotations on proofs and commenting on these marks.

Allows shapes, lines and freeform annotations to be drawn on proofs and for comment to be made on these marks..

How to use it

- Click on one of the shapes in the Drawing Markups section.
- Click on the proof at the relevant point and draw the selected shape with the cursor.
- To add a comment to the drawn shape, move the cursor over the shape until an arrowhead appears.
- Double click on the shape and type any text in the red box that appears.

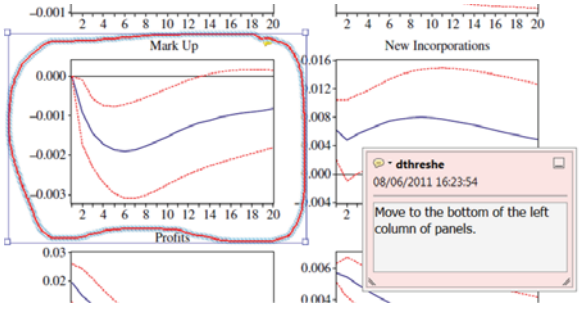

For further information on how to annotate proofs, click on the Help menu to reveal a list of further options: